Cubic–tetragonal–orthorhombic phase transition sequence in $0.5PbMg_{1/3}Nb_{2/3}O_3$–$0.5PbTiO_3$ and $0.36PbMg_{1/3}Nb_{2/3}O_3$–$0.64PbTiO_3$ single crystals

2006 J. Phys.: Condens. Matter 18 9625

(http://iopscience.iop.org/0953-8984/18/42/009)

INSTITUTE OF PHYSICS PUBLISHING JOURNAL OF PHYSICS: CONDENSED MATTER

J. Phys.: Condens. Matter **18** (2006) 9625–9641 doi:10.1088/0953-8984/18/42/009

Cubic–tetragonal–orthorhombic phase transition sequence in $0.5PbMg_{1/3}Nb_{2/3}O_3$–$0.5PbTiO_3$ and $0.36PbMg_{1/3}Nb_{2/3}O_3$–$0.64PbTiO_3$ single crystals

A Kania[1], **Ph Daniel**[2] **and A Słodczyk**[1,2]

[1] A Chełkowski Institute of Physics, University of Silesia, ulica Uniwersytecka 4. Pl 40-007 Katowice, Poland
[2] Laboratoire de Physique de l'Etat Condensé, (UMR CNRS No. 6087), Université du Maine Avenue O Messiaen, 72-085 Le Mans Cedex 9, France

Received 29 March 2006
Published 5 October 2006
Online at stacks.iop.org/JPhysCM/18/9625

Abstract

X-ray powder diffraction, Raman scattering and dielectric studies of $0.5PbMg_{1/3}Nb_{2/3}O_3$–$0.5PbTiO_3$ (0.5PMN–0.5PT) and $0.36PbMg_{1/3}Nb_{2/3}O_3$–$0.64PbTiO_3$ (0.36PMN–0.64PT) single crystals were carried out over a wide temperature range. The structural investigations revealed the existence of two structural phase transitions. The first one, from the paraelectric cubic ($Pm\bar{3}m$) to the ferroelectric tetragonal ($P4mm$) phase, occurs at 505 and 575 K for 0.5PMN–0.5PT and 0.36PMN–0.64PT, respectively. The second one, from the tetragonal to orthorhombic ferroelectric ($Pmm2$) phase, is observed at 292 K for 0.5PMN–0.5PT and at 235 K for 0.36PMN–0.64PT. The Raman investigations confirmed the existence of those phase transitions. The lowest frequency mode behaves like a soft mode. The dielectric investigations showed a sharp maximum of $\varepsilon'(T)$ at T_C, characteristic for normal ferroelectrics. Some evidence of the tetragonal–orthorhombic phase transition was detected by the dielectric and pyroelectric studies of only the polarized samples.

1. Introduction

Lead magnesium niobate–lead titanate solid solutions $(1-x)PbMg_{1/3}Nb_{2/3}O_3$–$xPbTiO_3$, i.e. $(1-x)$PMN–xPT or PMN–PT, formed between the relaxor $PbMg_{1/3}Nb_{2/3}O_3$ (PMN) and the ferroelectric $PbTiO_3$ (PT) have been intensively studied for almost two decades due to their excellent dielectric, electrostrictive and piezoelectric properties [1–4]. The PMN–PT system exhibits a great variety of physical behaviour and, therefore, is also very interesting from the fundamental point of view. Despite very intensive research these materials require additional studies since the results obtained by different authors and their interpretation are not fully consistent and in consequence many of the PMN–PT properties still remain unclear.

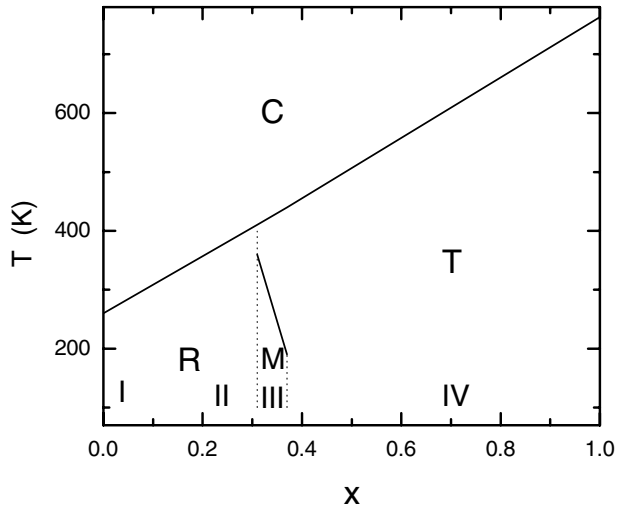

Figure 1. Schematic sketch of $(1-x)$PMN–xPT phase diagram proposed by Noheda *et al* (extended to $x = 0$ and $x = 1$ using the results of Ohwa *et al*). C, R, M and T denote the cubic, rhombohedral, monoclinic and tetragonal symmetries, respectively.

The PMN–PT phase diagram has been proposed by different authors [5–11]. There are some discrepancies between them relating mainly to the concentration ranges of the particular phase existences. However, most of them show a similar sequence of phases versus PT content. According to the currently accepted zero-field $(1 - x)$PMN–xPT phase diagram [7], shown in figure 1, four characteristic regions with different physical properties can be distinguished:

- Region I—including pure PMN and the solid solutions with PT content lower than 0.05 [12].
- Region II—so-called rhombohedral region specific for the solid solutions with PT concentration from 0.05 to 0.30.
- Region III—the morphotropic phase boundary (MPB) region including the solid solutions with PT content from 0.31 to 0.37.
- Region IV—so-called tetragonal region for the compositions with PT content higher than 0.38.

Most studies have focused on the solid solutions from the regions I, II and III because they exhibit relaxor behaviour (I and II) and giant piezoelectricity (III). Therefore, a very limited number of papers describing the compounds from region IV have been published [5–7, 9–14]. The authors of the available papers showed that the solid solutions from this region exhibit typical ferroelectric behaviour. At the Curie temperature T_C, these materials undergo a structural phase transition from the paraelectric cubic ($Pm\bar{3}m$) phase to the ferroelectric tetragonal ($P4mm$) one similar to $PbTiO_3$. The corresponding maximum of dielectric permittivity is sharp and frequency independent. However, recent single-crystal optical studies of 0.53PMN–0.47PT pointed to the possibility of an additional phase transition near 450 K [9, 10]. It is worth noting here that Kobayashi *et al* [15–17] found an additional low-temperature tetragonal–orthorhombic phase transition in pure $PbTiO_3$ crystals. This additional phase transition, also predicted theoretically [18], has not been confirmed by later studies and thus its existence requires clarification.

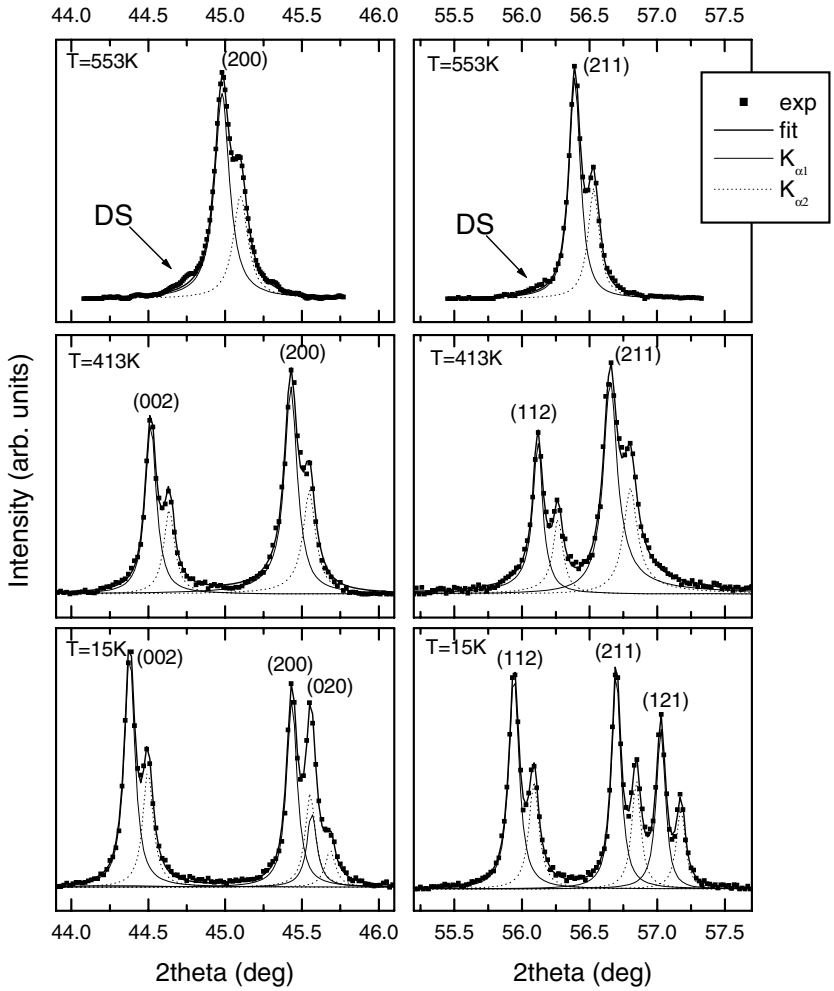

Figure 2. Temperature evolutions of the (200) and (211) Bragg reflections for 0.5PMN–0.5PT. DS denotes diffuse scattering.

The appearance of the soft mode in PMN–PT and $(1-x)PbZn_{1/3}Nb_{2/3}O_3$–$xPbTiO_3$ (PZN–PT) systems is one of the most important basic problems. Inelastic neutron scattering [19–22] and IR studies [23] of these materials with small PT content showed the presence of the transverse optic soft mode. However, the soft mode was not found in numerous Raman experiments performed for solid solutions of similar composition [11, 24–35]. In $PbTiO_3$ the soft mode was clearly observed by Raman scattering [36–40]. Therefore, one can expect soft mode appearance in the PMN–PT and PZN–PT solid solutions with high PT content.

Here we present complementary structural, vibrational and dielectric investigations of 0.5PMN–0.5PT and 0.36PMN–0.64PT single crystals over a wide temperature range.

2. Experimental methods

PMN–PT single crystals were grown by the flux method. The PbO–Pb_3O_4–B_2O_3 system was used as a solvent. Yellow, transparent and rectangular shaped single crystals of size up to

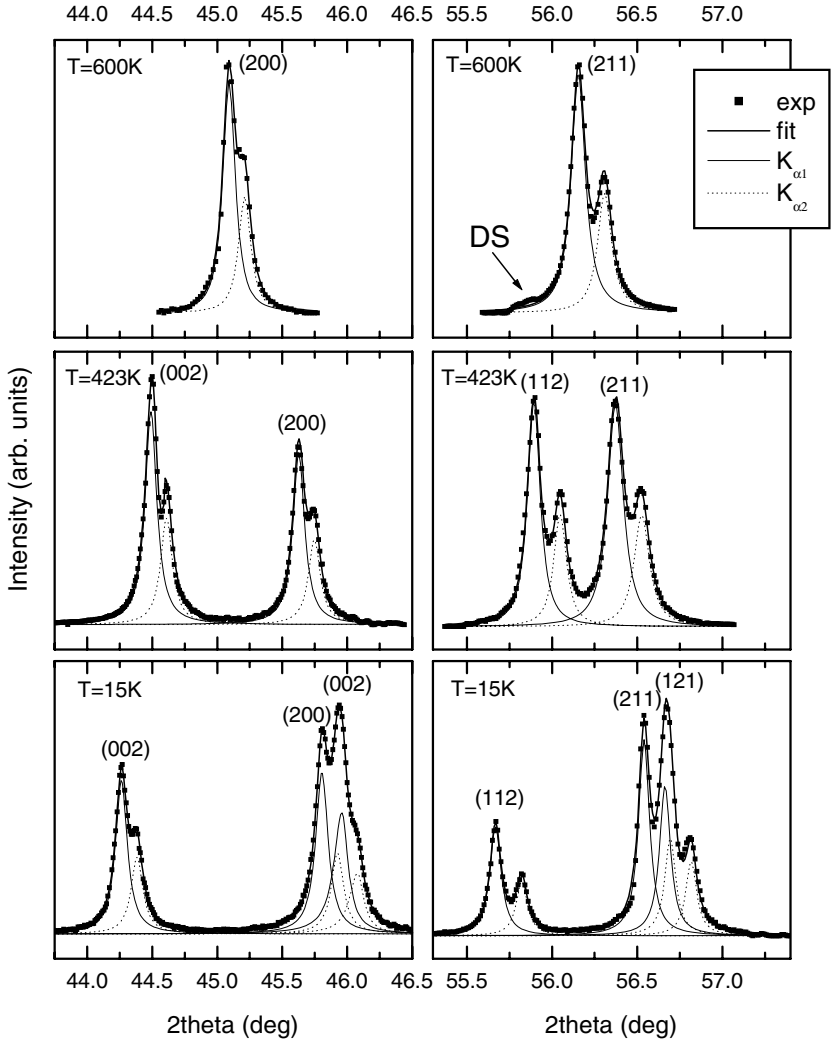

Figure 3. Temperature evolutions of the (200) and (211) Bragg reflections for 0.36PMN–0.64PT. DS denotes diffuse scattering.

$3 \times 3 \times 2$ mm^3 were obtained. Energy dispersion x-ray spectroscopy (EDS) using a scanning electron microscope (JSM-5410 JEOL) allowed us to determine the actual crystal composition. More details of the technological process of the crystal growth are given elsewhere [41].

X-ray powder diffraction measurements were performed using a high-resolution Siemens D5000 diffractometer (Bragg–Brentano $\theta/2\theta$ geometry, Cu Kα radiation filtered using Ni, $V = 40$ kV and $I = 30$ mA). Low-temperature measurements were carried out using a two-stage closed-cycle refrigerator He-TTK (Anton Paar). The sample holder was attached to the cold head by a flexible mesh providing good thermal conductance. An HTK1200 (Anton Paar) camera was used in the high-temperature experiments. In order to determine the crystal symmetry and the temperature of the phase transitions scans ($|\Delta(2\theta)| = 0.01^\circ$, 10 s counts per step) of selected Braggs reflections, (100), (110), (111), (200), (220), and (211), were

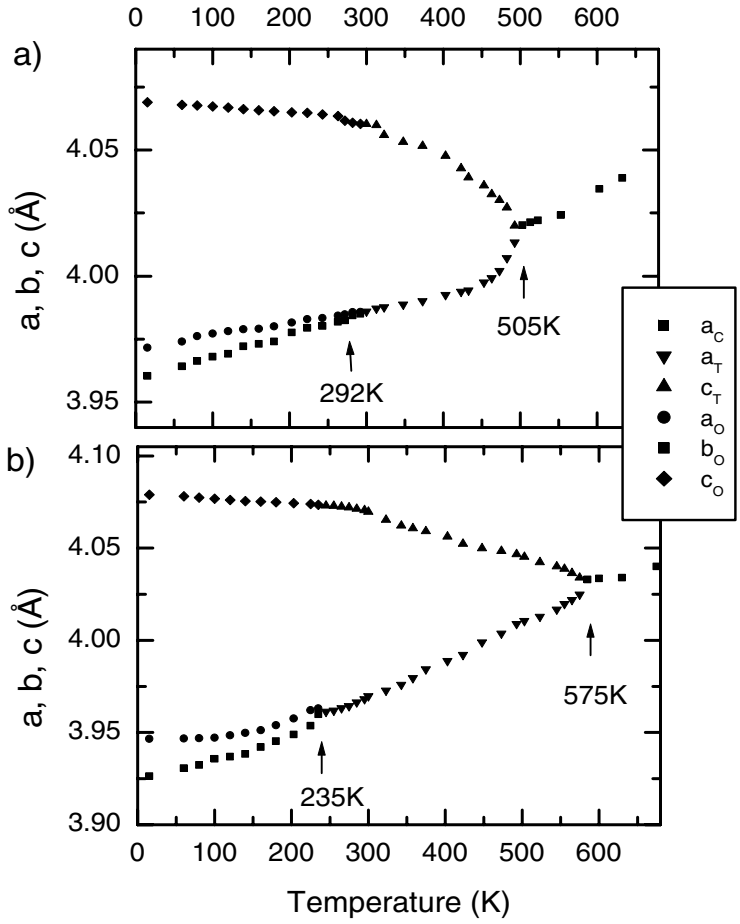

Figure 4. Temperature evolutions of the lattice parameters of (a) 0.5PMN–0.5PT and (b) 0.36PMN–0.64PT solid solutions.

collected over a wide temperature range. Additionally, at a few selected temperatures the full diffraction patterns in the range 18°–120° were recorded using a scanning method with a step $|\Delta(2\theta)| = 0.02°$ with 10 s counts per step. For these temperatures, crystal structure refinements were performed using the profile Rietveld method by means of the FullProf software [42].

Raman spectra were collected using a T64000 Yvon-Jobin multichannel triple monochromator spectrometer with a CCD detector (micro-Raman configuration, backscattering geometry). The 488 and 514 nm argon ion laser excitation lines were selected. The measurements were performed over the temperature range 77–700 K. The Raman spectra were recorded in the 25–1000 cm^{-1} range. The Peakfit software program [43] was used to deconvolute the overlapping modes and to determine the line parameters: integrated intensity, frequency and line width.

Samples for the dielectric measurements were cut parallel to the (100) natural faces, polished and electroded with silver paste. Dielectric measurements were performed using an HP 4263B LCR meter for frequencies 0.1, 1, 10 100 kHz and measuring field equal to 20 V cm^{-1}. Measurements were carried out over the temperature range 110–600 K.

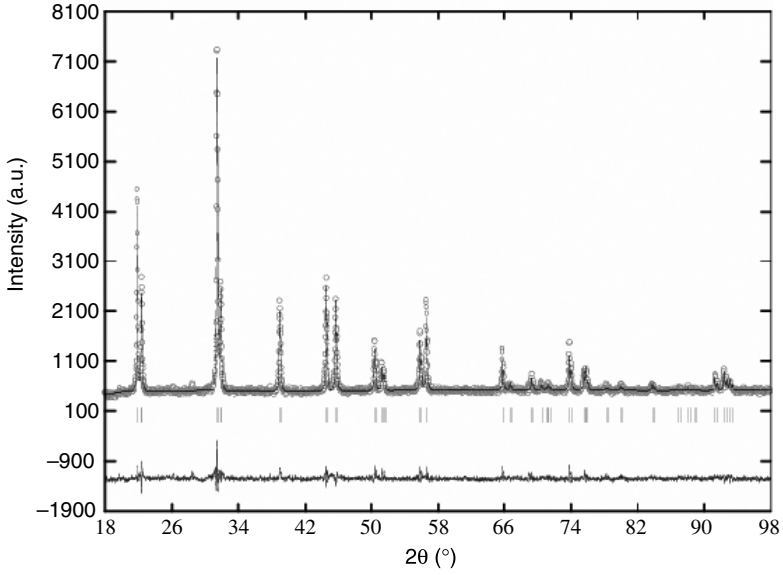

Figure 5. The Rietveld refined pattern of 0.36PMN–0.64PT at 300 K (open circles mark the experimental data and the continuous line the calculated pattern while the bottom line shows the differences between them).

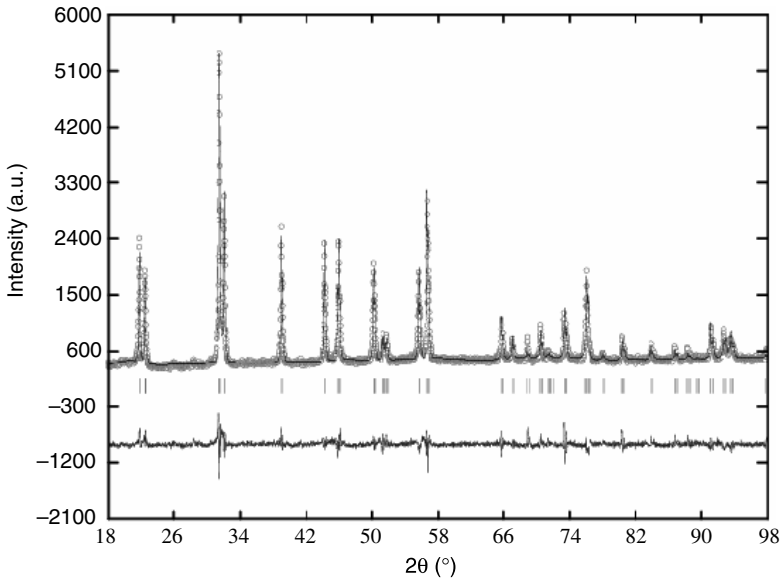

Figure 6. The Rietveld refined pattern of 0.36PMN–0.64PT at 15 K (open circles mark the experimental data and the continuous line the calculated pattern while the bottom line shows the differences between them).

3. Results and discussion

3.1. X-ray diffraction results

The temperature evolutions of the (200) and (211) Bragg reflections of 0.5PMN–0.5PT and 0.36PMN–0.64PT are shown in figures 2 and 3, respectively. These evolutions are very similar.

Table 1. Results of the crystal structure refinements for 0.36PMN–0.64PT at 623, 300 and 15 K.

Temperature = 623 (K)			Space group: $Pm\bar{3}m$	
$R_{Bragg} = 7.73\%$			$a = 4.0339(3)$ Å	
$R_F = 7.49\%$				
Ions	x	y	z	B^{iso} (Å)^2
Pb^{2+}	0	0	0	3.55(3)
$Mg^{2+}/Nb^{5+}/Ti^{4+}$	0.5	0.5	0.5	1.55(4)
O^{2-}	0.5	0.5	0	2.08(1)
Temperature = 300 (K)			Space group: *P4mm*	
$R_{Bragg} = 6.31\%$			$a = 3.9696(1)$ Å	
$R_F = 6.33\%$			$c = 4.0696(2)$ Å	
Ions	x	y	z	B^{iso} (Å)^2
Pb^{2+}	0	0	0	2.54(3)
$Mg^{2+}/Nb^{5+}/Ti^{4+}$	0.5	0.5	0.538(2)	1.11(2)
O_I^{2-}	0.5	0	0.613(4)	1.34(3)
O_{II}^{2-}	0.5	0.5	0.109(2)	1.23(4)
			Space group: *Pmm2*	
Temperature = 15 (K)			$a = 3.9464(2)$ Å	
$R_{Bragg} = 5.81\%$			$b = 3.9263(3)$ Å	
$R_F = 6.13\%$			$c = 4.0788(2)$ Å	
Ions	x	y	z	B^{iso} (Å)^2
Pb^{2+}	0	0	0	1.41(4)
$Mg^{2+}/Nb^{5+}/Ti^{4+}$	0.5	0.5	0.544(2)	0.59(3)
O_I^{2-}	0.5	0	0.618(3)	0.75(2)
O_{II}^{2-}	0.5	0.5	0.117(4)	0.78(2)
O_{III}^{2-}	0	0.5	0.488(2)	0.72(1)

At high temperatures all reflections are single, which points to the presence of cubic symmetry. On cooling, at 505 K (0.5PMN–0.5PT) and 575 K (0.36PMN–0.64PT) the abrupt splitting of most of the Bragg reflections, characteristic for tetragonal symmetry, is observed. With further temperature decrease, an additional splitting characteristic of orthorhombic symmetry appears at 292 and 235 K for 0.5PMN–0.5PT and 0.36PMN–0.64PT, respectively. In contrast to the cubic–tetragonal phase transition the tetragonal–orthorhombic one goes more smoothly. However, it should be stated that the multiplets characteristic for the orthorhombic symmetry develop over several degrees. With further cooling the line splitting becomes more distinct and simultaneously the lines become narrower. This suggests that the possibility of coexistence of the tetragonal and orthorhombic phases at low temperatures should not be considered. The presence of orthorhombic symmetry in region IV is, to the best of our knowledge, reported here for the first time.

The temperature dependences of the lattice parameters of 0.5PMN–0.5PT and 0.36PMN–0.64PT are presented in figure 4. These dependences point to the presence of two structural phase transitions. For both crystals the sharp cubic–tetragonal transformation exhibits the nature of a first-order phase transition.

The analysis of the diffraction patterns of both 0.5PMN–0.5PT and 0.36PMN–0.64PT crystals revealed additionally the presence of diffuse scattering (near $\{h00\}$, $\{hh0\}$ and $\{hkk\}$ reflections) only within the cubic phase (figures 2 and 3). It is quite a different feature to that

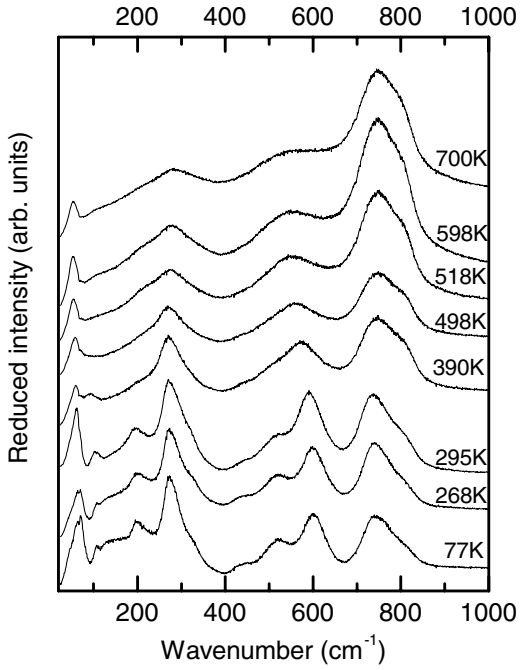

Figure 7. Raman spectra of 0.5PMN–0.5PT single crystals recorded at different temperatures.

found in the PMN–PT solid solutions from regions I–III, for which the diffuse scattering related to polar nanoregions (PNRs) appears for all phases [7, 30, 44–46]. This allows us to assume that nanoregions of symmetry different from cubic appear above the cubic–tetragonal transition. We suggest that the symmetry of these nanoregions should be the same as the symmetry which appears after the structural phase transition, i.e. tetragonal with the *P4mm* space group.

The crystal structure refinements were performed for diffraction patterns recorded at selected temperatures from cubic, tetragonal and orthorhombic phases, namely at 603, 453 and 15 K for 0.5PMN–0.5PT and 623, 300 and 15 K for 0.36PMN–0.64PT. The best agreements between the experimental data and the theoretical models were achieved using the $Pm\bar{3}m$, *P4mm* and *Pmm2* space groups for cubic, tetragonal and orthorhombic symmetry, respectively. The $Pm\bar{3}m$ and *P4mm* space groups are the same as in pure PT while the *Pmm2* space group corresponds to the hypothetical orthorhombic symmetry in PT [15–18]. Figures 5 and 6 show examples of the Rietveld refinements for 0.36PMN–0.64PT. For the particular phases the determined crystal structures of both compounds are very similar and thus the refinement details only for 0.36PMN–0.64PT are listed in table 1.

The obtained reliability factors and isotropic thermal parameters are smaller than those known for the compounds from regions I–III [30, 45–48]. However, they are still high in comparison to the ordered materials. Their high values especially in the cubic phase confirm the presence of structural disorder in 0.5PMN–0.5PT and 0.36PMN–0.64PT single crystals.

3.2. Raman scattering results

We made several attempts to record polarized Raman spectra but unfortunately unsuccessfully. This was caused probably by the presence of a complex domain structure in the investigated crystals. Therefore in further investigations the unpolarized Raman spectra were

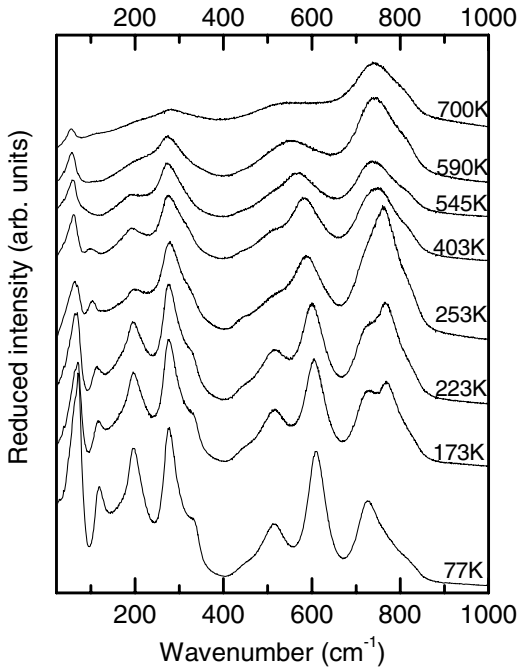

Figure 8. Raman spectra of 0.36PMN–0.64PT single crystals recorded at different temperatures.

collected. Figures 7 and 8 show temperature evolutions of the reduced (corrected by Bose–Einstein population factor) Raman spectra of 0.5PMN–0.5PT and 0.36PMN–0.64PT crystals, respectively. As in other complex perovskites, such as disordered $PbSc_{1/2}Ta_{1/2}O_3$ (PST) and $PbIn_{1/2}Nb_{1/2}O_3$ (PIN), as well as PZN–PT [31–35, 49–51], the first-order Raman spectrum appears in PMN–PT single crystals within the cubic paraelectric phase. This spectrum, forbidden for $Pm\bar{3}m$ space group, originates from nanoregions of different local symmetry. Usually, authors explain this Raman activity by the presence of regions of $Fm\bar{3}m$ symmetry, which appears due to the 1:1 chemical order in the B-ion sublattice. However, as was experimentally evidenced, this origin of the high-temperature Raman activity in PMN–PT and PZN–PT solid solutions is valid only for compounds with Ti content smaller than 0.25 [11, 45]. Therefore, for materials with higher PT content we proposed to connect this Raman activity with polar nanoregions of the same symmetry as the symmetry of the low-temperature phase, i.e. rhombohedral for $0.21 \leqslant x \leqslant 0.28$ and tetragonal for $x > 0.32$ [46].

As is clearly shown in figures 7 and 8, no drastic changes of the Raman spectra versus temperature are observed. With the decrease of temperature the line becomes narrower and in the vicinity of the structural phase transitions some lines split and new weak lines appear. The quantitative temperature evolutions of Raman spectrum can be determined only after calculations are made. A model of independent damped oscillators was employed:

$$I(\omega) = \frac{S_i \Gamma_i \omega_{i0}^2 \omega}{(\omega^2 - \omega_{i0}^2)^2 + \Gamma_i^2 \omega_{i0}^2}(n(\omega) + 1)$$

where S_i, Γ_i and ω_{i0} are the intensity factor, damping constant and the mode frequency, respectively, and $n(\omega)$ is the Bose–Einstein population factor.

The calculations showed that deconvolutions of the Raman spectra of both investigated compounds are very similar for the particular phases. Therefore, figure 9 shows these

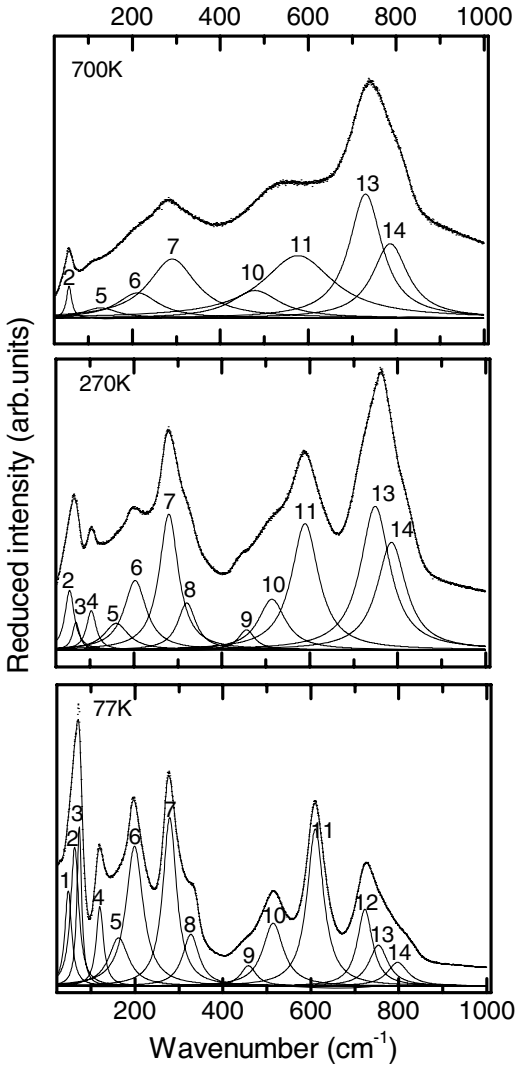

Figure 9. Deconvolution of the Raman spectra of 0.36PMN–0.64PT crystal at selected temperatures.

deconvolutions for 0.36PMN–0.64PT single crystals only. The Raman spectra recorded at 700 K can be well decomposed into 8 lines and they may be connected with polar nanoregions of tetragonal symmetry (*P4mm*). Most of these Raman lines are undoubtedly of first order. The Raman spectra recorded within the tetragonal (270 K) and orthorhombic (77 K) phases can be well decomposed into 12 and 14 lines, respectively. Group theory analysis predicts 8 active Raman lines for the tetragonal (*P4mm*) symmetry and 12 lines for the orthorhombic (*Pmm2*) one (table 2). In our opinion the discrepancies between the numbers of predicted and observed Raman modes cannot be explained by the coexistence of phases, because such a coexistence was not found in the structural studies. The splitting of the Raman modes into TO (transverse optic) and LO (longitudinal optic) lines due to the long-range electrostatic forces, as in pure PT [30–34], seems to be a more reliable explanation of these discrepancies. Within

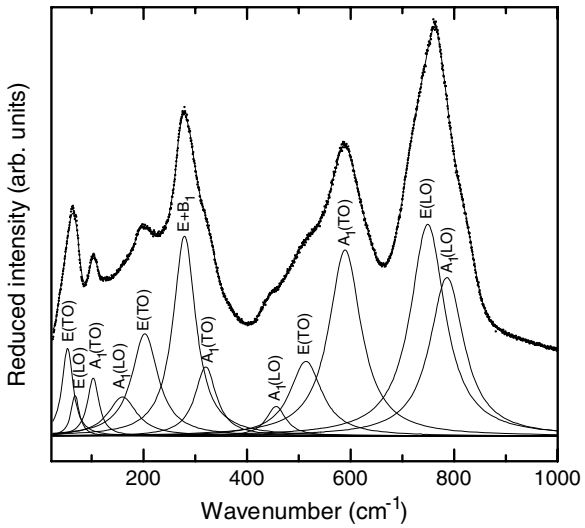

Figure 10. The proposed assignment of the Raman modes observed at 270 K for 0.36PMN–0.64PT.

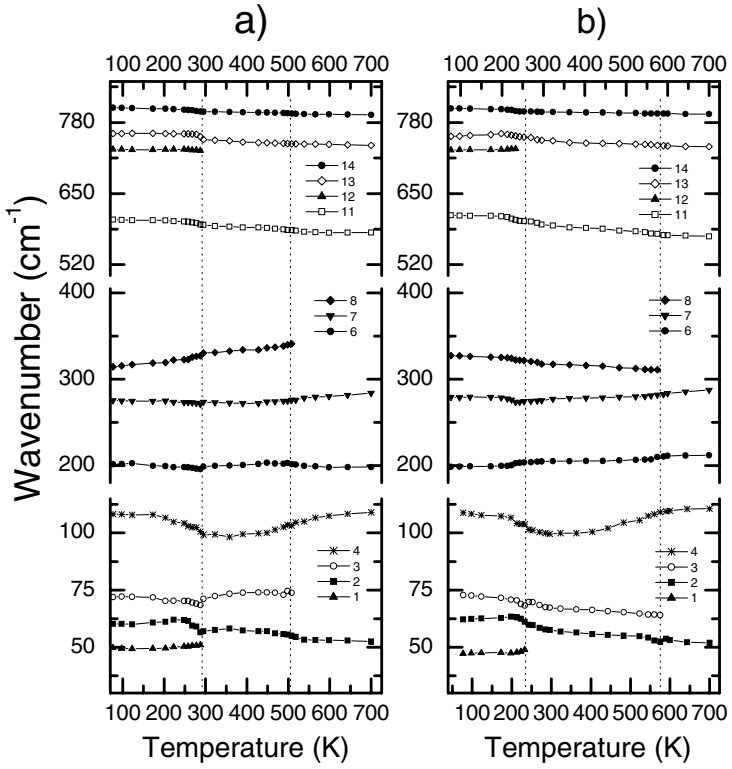

Figure 11. Temperature dependences of the frequency of Raman lines for (a) 0.5PMN–0.5PT and (b) 0.36PMN–0.64PT.

the ferroelectric tetragonal phase of PT, the following Raman modes are observed: 3E(TO), 3E(LO), $3A_1$(TO), $3A_1$(LO) and $B_1 + E$ [36–40]. Therefore, since the Raman spectra of

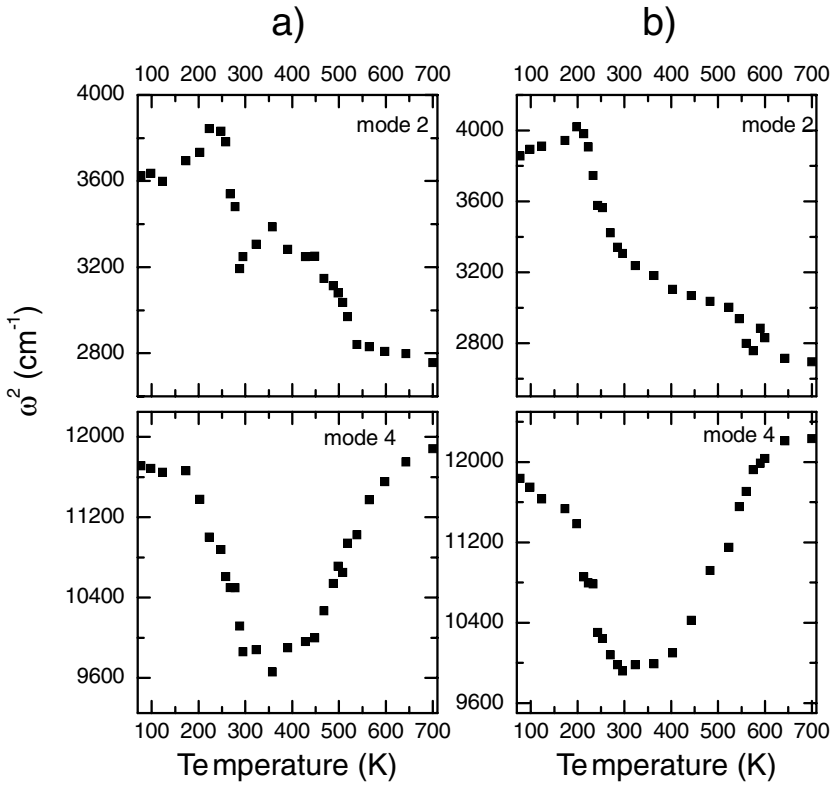

Figure 12. Temperature dependences of the frequency square ω^2 of line 2 and line 4 for (a) 0.5PMN–0.5PT and (b) 0.36PMN–0.64PT single crystals.

Table 2. Group theory analysis for symmetries observed in the 0.5PMN–0.5PT and 0.36PMN–0.64PT. (Calculations were performed using the site symmetry method at the centre of Brillouin zone: Γ point = (0, 0, 0).)

Symmetry	Γ_{total}	Γ_{Raman}
O_h^1 ($Pm\bar{3}m$)	$\Gamma = 3F_{1u} + F_{2u} + F_{1u}$	$\Gamma_{\text{Raman}} = 0$
C_{4v}^1 ($P4mm$)	$\Gamma = 4A_1 + B_1 + 5E$	$\Gamma_{\text{Raman}} = 3A_1 + B_1 + 4E$
C_{2v}^1 ($Pmm2$)	$\Gamma = 5A_1 + 5B_1 + 5B_2$	$\Gamma_{\text{Raman}} = 4A_1 + 4B_1 + 4B_2$

0.50PMN–0.50PT and 0.36PMN–0.64PT were recorded for crystals with the multi-domain state, the number of the observed lines seems to be in good agreement with the TO–LO prediction. It must be pointed out that the interpretation of the Raman spectra based on the TO–LO splitting has been also used in the case of similar materials like $PbZr_{1-x}Ti_xO_3$ (PZT), Nd-doped PZT and $Pb_{1-y}La_{2y/3}Zr_{1-x}Ti_xO_3$ (PLZT) [52–55]. Figure 10 shows the proposed assignment of the Raman lines of 0.36PMN–0.64PT at 270 K done by analogy to PT [36–40]. In comparison with pure PT most of the Raman modes are shifted towards lower frequencies.

Figure 11 presents the temperature dependences of the calculated mode frequencies for the investigated crystals. In the vicinity of the cubic–tetragonal phase transition some new lines appear, while near the tetragonal–orthorhombic phase transition two lines split. The frequency of the majority of the lines does not depend strongly on temperature. The frequency of only two lines, 2 and 4, depends significantly on temperature and for these two lines the frequency square

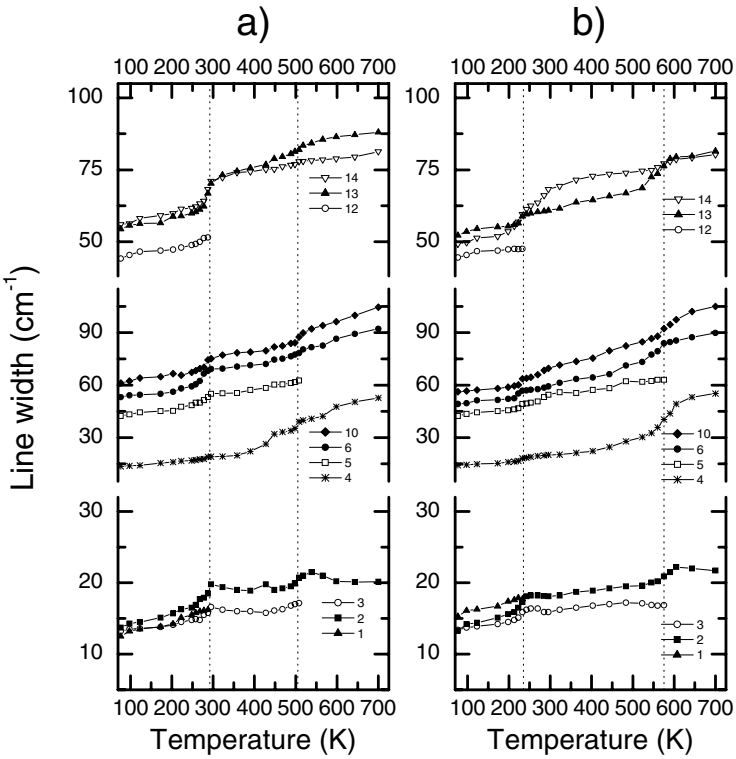

Figure 13. Temperature dependences of the line widths of selected Raman lines for (a) 0.5PMN–0.5PT and (b) 0.36PMN–0.64PT.

ω^2 versus temperature is plotted in figure 12. The lowest frequency mode (2) exhibits similar behaviour to the soft mode in pure PT. The frequency of this mode decreases with increasing temperature and reaches its lowest value in the vicinity of the cubic–tetragonal phase transition. The frequency of mode 4 reaches a minimum value near the tetragonal–orthorhombic phase transition.

The temperature evolutions of the line width of the selected Raman lines are shown in figure 13. For all modes the line width decreases with decrease in temperature. However, for some low-frequency lines a small increase of the line width is observed in the vicinity of the phase transitions. These lines are connected with the Pb vibrations and thus the observed anomalies of the line widths may indicate a special role of Pb ions in the phase transition mechanism.

3.3. Results of dielectric investigations

Figure 14 presents the temperature dependences of the real ε' and imaginary ε'' parts of the dielectric permittivity for 0.5PMN–0.5PT and 0.36PMN–0.64PT single crystals. Due to a significant increase of electric conductivity and two-layered capacitor appearance at high temperatures the large increase of the value of the dielectric constant and dielectric losses are measured for low frequencies. They do not reflect the true dielectric properties of the material. Therefore, figure 14 presents these dependences only for the highest frequencies used (10 and 100 kHz). As is clearly seen, both investigated crystals exhibit classical ferroelectric behaviour

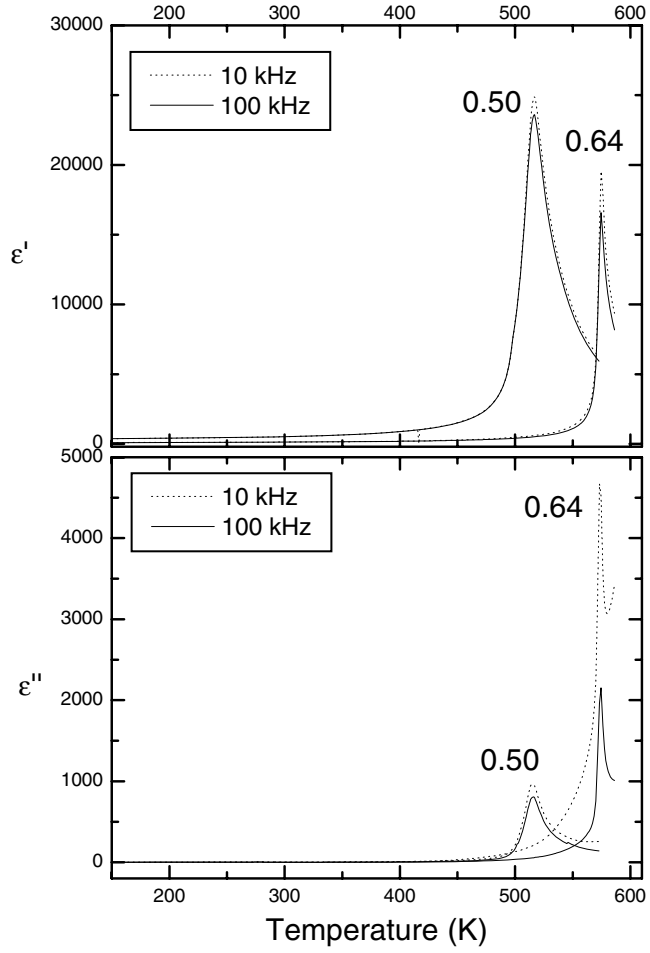

Figure 14. Temperature dependences of the real ε' and imaginary ε'' parts of the dielectric permittivity for 0.5PMN–0.5PT and 0.36PMN–0.64PT, on heating.

with a sharp and narrow $\varepsilon(T)$ maximum at the Curie temperature T_C (cubic–tetragonal phase transition). The temperatures of $\varepsilon(T)$ maxima do not depend on frequency, and dielectric dispersion within the ferroelectric phase is not significant.

In contrast to the cubic tetragonal phase transition, the $\varepsilon'(T)$ and $\varepsilon''(T)$ dependences for both investigated compounds do not indicate the tetragonal–orthorhombic phase transition at all. This may mean that this phase transition occurs as a continuous transformation between the tetragonal and orthorhombic structures. The temperature evolutions of the lattice parameters also point to such behaviour. Dielectric properties in the vicinity of the orthorhombic-tetragonal phase transition were measured also for polarized samples. At 390 K an electric field of strength 3 kV cm^{-1} was applied and then the sample was cooled to 120 K. At this temperature the electric field was taken off and the sample was kept for one hour at this temperature. Dielectric measurements were performed on heating to 380 K (ZFH_FC) and then on cooling (ZFC_FC). The results of these measurements (ZFC_FC) as well as the measurements of the unpolarized (ZFC) 0.5PMN–0.5PT sample are shown in figure 15. These dependences show that only the $\varepsilon''(T)$ dependence exhibits a very weak anomaly in the vicinity of the tetragonal–orthorhombic

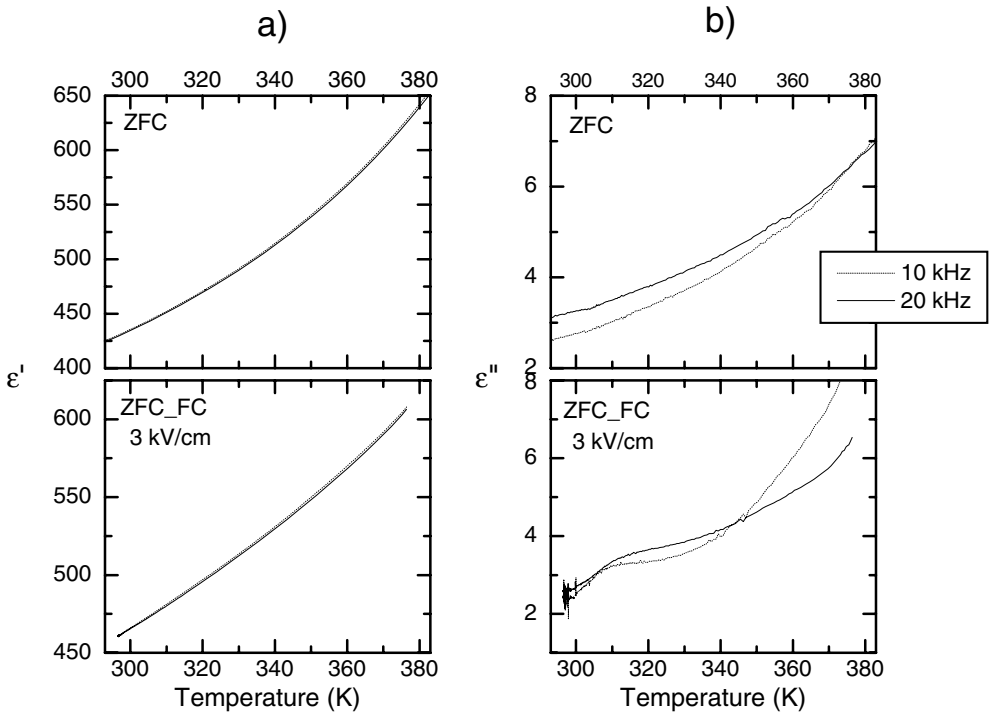

Figure 15. Comparison of temperature dependences of the real ε' and imaginary ε'' parts of the dielectric permittivity measured in ZFC and ZFC_FC conditions for 0.5PMN–0.5PT.

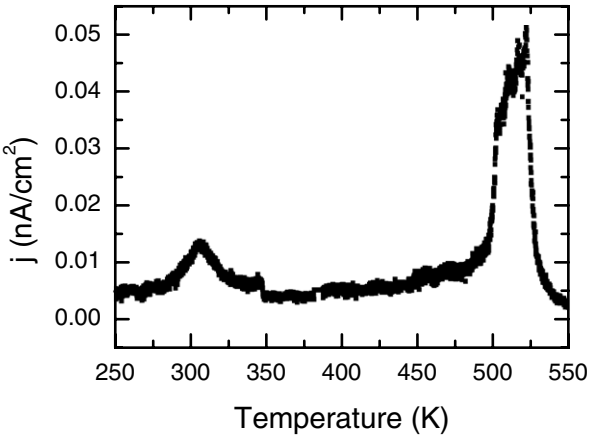

Figure 16. Density of pyroelectric current versus temperature for 0.5PMN–0.5PT.

transition. The results of similar experiments performed for the polarized 0.36PMN–0.64PT sample did not show clear evidence of the tetragonal–orthorhombic phase transition.

For crystals of 0.5PMN–0.5PT polarized in the way described above, a pyroelectric effect was investigated. Figure 16 presents the density of the pyroelectric current versus temperature. Two maxima related to the changes of spontaneous polarization are clearly seen and thus they indicate the presence of two structural phase transitions.

4. Conclusions

X-ray powder diffraction, Raman scattering and dielectric studies of 0.5PMN–0.5PT and 0.36PMN–0.64PT single crystals were performed over a wide temperature range. These complementary investigations revealed the existence of a cubic–tetragonal–orthorhombic phase transition sequence in these materials. The first phase transition, from the paraelectric cubic phase ($Pm\bar{3}m$) to the ferroelectric tetragonal phase ($P4mm$), is observed at 505 K for 0.5PMN–0.5PT and at 575 K in the case of 0.36PMN–0.64PT. The second one, from the tetragonal to orthorhombic ferroelectric ($Pmm2$) phase, occurs at 292 and 235 K for 0.5PMN–0.5PT and 0.36PMN–0.64PT, respectively.

First-order Raman spectra are observed over the whole measured temperature range. We suggest that the high-temperature Raman spectrum, forbidden by $Pm\bar{3}m$ symmetry, originates from nanoregions with tetragonal symmetry. The Raman lines observed within the tetragonal and orthorhombic symmetries can be explained by TO–LO splitting. Two low-frequency modes exhibit soft-mode-like behaviour. The dielectric investigations showed that 0.5PMN–0.5PT and 0.36PMN–0.64PT single crystals behave as normal ferroelectrics. They exhibit a sharp, frequency-independent maximum of $\varepsilon'(T)$ at T_C. The dielectric measurements do not show the tetragonal–orthorhombic phase transition clearly. Some evidence of this phase transition can be detected in the dielectric and pyroelectric studies of polarized crystals only.

References

[1] Cross L E 1987 *Ferroelectrics* **76** 241
[2] Park S-E and Shrout T R 1997 *J. Appl. Phys.* **82** 1804
[3] Park S-E and Shrout T R 1997 *Mater. Res. Innov.* **1** 20
[4] Fu H and Cohen R H 2000 *Nature* **403** 281
[5] Choi W, Shrout T R, Jang S J and Bhalla A S 1989 *Ferroelectrics* **100** 29
[6] Noblanc O, Gaucher P and Calvarin G 1996 *J. Appl. Phys.* **79** 4291
[7] Noheda B, Cox D E, Shirane G, Ye Z G and Gao J 2002 *Phys. Rev.* B **66** 054104
[8] Gehring P M, Chen W, Ye Z G and Shirane G 2004 *J. Phys.: Condens. Matter* **16** 7113
[9] Zekria D, Shuvaeva V A and Glazer A M 2005 *J. Phys.: Condens. Matter* **17** 1593
[10] Shuvaeva V A, Glazer A M and Zekria D 2005 *J. Phys.: Condens. Matter* **17** 5709
[11] Ohwa H, Iwata M, Orihara H, Yasuda N and Ishibashi Y 2001 *J. Phys. Soc. Japan* **70** 3149
[12] Ye Z G, Bing Y, Gao J, Bokov A A, Stephens P, Noheda B and Shirane G 2003 *Phys. Rev.* B **67** 104104
[13] Ye Z-G and Dong M 2004 *J. Appl. Phys.* **96** 1620
[14] Cao H, Schmidt V H, Zhang R, Cao W and Luo H 2000 *J. Appl. Phys.* **87** 2312
[15] Kobayashi J and Ueda R 1955 *Phys. Rev.* **99** 1900
[16] Kobayashi J, Okamoto S and Ueda R 1956 *Phys. Rev.* **103** 830
[17] Kobayashi J, Uesu Y and Sakemi Y 1983 *Phys. Rev.* B **28** 3866
[18] Garcia A and Vanderbilt D 1996 *Phys. Rev.* B **54** 3817
[19] Gehring P M, Park S E and Shirane G 2000 *Phys. Rev. Lett.* **84** 5216
[20] Gehring P M, Wakimoto S, Ye Z G and Shirane G 2001 *Phys. Rev. Lett.* **87** 277601
[21] Gehring P M, Park S E and Shirane G 2001 *Phys. Rev.* B **63** 224109
[22] Wakimoto S, Stock C, Birgeneau R J, Ye Z G, Chen W, Buyers W J, Gehring P M and Shirane G 2002 *Phys. Rev.* B **65** 172105
[23] Kamba S, Kempa M, Bovtun V, Petzelt J, Brinkman K and Setter N 2005 *J. Phys.: Condens. Matter* **17** 3965
[24] Husson E, Abello L and Morell A 1990 *Mater. Res. Bull.* **25** 539
[25] Idink H and White W 1994 *J. Appl. Phys.* **76** 1789
[26] Siny I G, Lushnikov S G, Katiyar R S and Rogacheva E A 1997 *Phys. Rev.* B **56** 7962
[27] Marsi M El, Farhi R and Yuzyuk Yu 1998 *J. Phys.: Condens. Matter* **10** 9161
[28] Svitelskiy O, Toulouse J, Yong G and Ye Z G 2003 *Phys. Rev.* B **68** 104107
[29] Kamba S, Buixaderas E, Petzelt J, Fousek J, Nosek J and Bridenbaugh P 2003 *J. Appl. Phys.* **93** 933
[30] Slodczyk A, Kania A, Daniel Ph and Ratuszna A 2005 *J. Phys. D: Appl. Phys.* **38** 2910

[31] Iwata M, Tomisato N, Orihara H, Arai N, Tanaka N, Ohwa H, Yasuda N and Ishibashi Y 2001 *Japan. J. Appl. Phys.* **40** 5819
[32] Lebon A, Marssi M El, Farhi R, Dammak H and Calvarin G 2001 *J. Appl. Phys.* **89** 3947
[33] Kim S, Yang I S, Lee J K and Hong K S 2001 *Phys. Rev.* B **64** 094105
[34] Svitelskiy O, La-Orauttapong D, Toulouse J, Chen W and Ye Z G 2005 *Phys. Rev.* B **72** 1172106
[35] Toulouse J, Jiang F, Svitelskiy O, Chen W and Ye Z G 2005 *Phys. Rev.* B **72** 184106
[36] Burns G and Scott B A 1970 *Phys. Rev. Lett.* **25** 167
[37] Burns G and Scott B A 1973 *Phys. Rev.* B **7** 3088
[38] Freire J D and Katiyar R S 1988 *Phys. Rev.* B **37** 2074
[39] Fontana M D, Idrissi H, Kugel G E and Wojcik K 1991 *J. Phys.: Condens. Matter* **3** 8695
[40] Foster C M, Li Z, Grimsditch M, Chan S K and Lam D J 1993 *Phys. Rev.* B **48** 10160
[41] Kania A, Slodczyk A and Ujma Z 2006 *J. Cryst. Growth* **289** 134
[42] Rodriguez-Carvajal J 2001 *Introduction to the Program Fullprof*
[43] Peakfit version 4.12 Copyright 2003 by Seasolve Software Inc, USA
[44] de Mathan N, Husson E, Calvarin G, Gavarri J R, Hewat A W and Morell A 1991 *J. Phys.: Condens. Matter* **3** 8159
[45] Dkhil B, Kiat J M, Calvarin G, Baldinozzi G, Vakhrushev S B and Suard E 2001 *Phys. Rev.* B **65** 024104
[46] Slodczyk A, Daniel Ph and Kania A 2006 *Phys. Rev.* B submitted
[47] Kiat J M, Uesu Y, Dkhil B, Matsuda M, Malibert Ch and Calvarin G 2002 *Phys. Rev.* B **65** 064106
[48] Singh A K and Pandey D 2003 *Phys. Rev.* B **67** 064102
[49] Bismayer U, Devarajan V and Groves P 1989 *J. Phys.: Condens. Matter* **1** 6977
[50] Boulesteix C, Caranoni C, Kang C Z, Sapozhnikova L S, Siny I G and Smirnova T A 1990 *Ferroelectrics* **107** 241
[51] Kania A, Roleder K, Kugel G E and Hafid M 1992 *Ferroelectrics* **135** 75
[52] Frantti J, Lantto V and Lappalainen J 1996 *J. Appl. Phys.* **79** 1065
[53] Marssi M El, Farhi R and Viehland D 1997 *J. Appl. Phys.* **81** 355
[54] Frantti J, Lantto V, Nishio S and Kakihama M 1996 *Japan. J. Appl. Phys.* **38** 5679
[55] Lima K C V, Souza Filho A G, Ayala A P, Mendes Filho J, Freire P T, Melo F E, Araujo E B and Eiras J A 2001 *Phys. Rev.* B **63** 184105